

# 4DFlowMRI Data Assimilation: Integrated approach reveals a potential biomarker in experimental ARDS condition.

Rahul Kumar<sup>1\*</sup>, Angel Gaítan Simon<sup>3</sup>, Ignacio Rodríguez<sup>3</sup>, María Jesús Sánchez Guisado<sup>1</sup>, Maialen Stephens<sup>5</sup>, Karen Lopez-Lináres Roman<sup>5</sup>, Jesus Ruiz Cabello<sup>1,2,3,4\*</sup>

<sup>1</sup>M&FB, CIC biomaGUNE, Paseo de Miramon 182, Donostia San Sebastián, 20014, Basque Country, Spain.

<sup>2</sup>BRTA, Basque Foundation for Science,, Plaza Euskadi 5, Donostia San Sebastián, 48009, Basque Country, Spain.

<sup>3</sup>NMR and Imaging in Biomedicine Group, Department of Chemistry in Pharmaceutical Sciences, Pharmacy School, University Complutense Madrid,, City, 28040, Madrid, Spain.

<sup>4</sup>Ciber Enfermedades Respiratorias (Ciberes), Street, Madrid, 28029, Madrid, Spain.

<sup>5</sup>Vicomtech, Parque Científico y Tecnológico de Gipuzkoa, Donostia / San Sebastián (Spain), 20009, Basque Country, Spain.

\*Corresponding author(s). E-mail(s): [rkumar@cicbiomagune.es](mailto:rkumar@cicbiomagune.es), [jruizcabello@cicbiomagune.es](mailto:jruizcabello@cicbiomagune.es);

## Abstract

Acute respiratory distress syndrome (ARDS) is a life threatening respiratory condition characterized by hypoxemia and stiff lungs. This paper presents a detailed CFD study of the porcine pulmonary artery for different spectrums of experimental ARDS combining imaging data from 4D-Flow MRI with hemodynamic pressure and flow waveforms from control and hypertensive pigs. Fluid dynamics equations are solved for the subject-specific pulmonary arterial network. The proposed novel biomarker offers a unique solution to decide the beneficial and detrimental values of certain PEEP levels through the use of an integrated approach. This biomarker showcases the potential to significantly impact the field of PVD and blood flow by effectively improving pulmonary vascular mechanics.

**Keywords:** ARDS, ASR, CFD, CFL, PVR, WSS, TAWSS, OSI, ASR, MS, MI, MPA, LPA, RPA, TAC, RV

## 1 Introduction

Acute respiratory distress syndrome (ARDS) in adults is characterized by the rapid onset of non-cardiogenic pulmonary edema, which is an abnormal accumulation of fluid in the extravascular compartments of the lungs leading to hypoxemia and lung collapse [1], which in turn compromise gas exchange. The relationships between driving pressure for blood flow and the cardiac output are governed by the active and passive changes in the pulmonary circulatory system. The increased flow resistance makes it difficult for the heart to pump blood to the lungs, adding strain to and weakening the right ventricle. The pulmonary vasculature is highly reactive to oxygen and the spectrum of pulmonary vascular dysfunction in ARDS ranges from mild PAH to Acute cor pulmonale, which can cause hemodynamic instability, a primary factor influencing mortality.

Hemodynamic instability is defined as perfusion failure that can manifest as advanced heart failure. Hemodynamic instability can be a significant factor contributing to mortality in critically ill patients, particularly in those with ARDS and other conditions that require mechanical ventilation. However, it is important to note that hemodynamic instability is only one of the many factors that can influence mortality in critically ill patients. Other factors, such as the underlying disease process, the patient's age and comorbidities, the presence of sepsis or other infections, and the overall response to therapy can also play important roles in determining clinical outcomes. While hemodynamic instability can be an important factor in determining mortality risk, it should be considered as part of a broader clinical picture and addressed in conjunction with other factors to optimize patient outcomes. The effect of lung volume on pulmonary vascular resistance is mainly due to mechanical effects which lead to increase in pressure and resistance within the pulmonary circulation. Mechanical ventilation challenges have been highlighted in the current COVID-19 pandemic, as the virus primarily affects the lung and can also affect the hemodynamics. Hemodynamic instability is a primary factor influencing mortality, and the mortality rate among COVID-19 ARDS ventilated patients is one of the most disheartening published results [2, 3].

Mechanical ventilation is a crucial practice in modern medicine and is used to protect lung structure and function in the management of patients with ARDS. It can have both beneficial and detrimental effects on hemodynamic instability, depending on various factors such as the patient's underlying cardiovascular status, the settings and mode of mechanical ventilation, and the presence of other comorbidities. Intermittent positive pressure ventilation changes the lung volume. The change in lung volume changes the pressure difference between the airway and the pleural pressure (**Fig. 1**). This pressure difference changes the pulmonary vascular resistance (PVR) as anything that over distends lung units increases vascular resistance and if it occurs globally throughout the lungs, it can increase PVR. Mechanical ventilation has a profound

effect on the cardiovascular system and can induce acute right ventricular failure if not properly performed. Hyperinflation is common when patients are over-ventilated. Different strategies are used without considering, in some cases, the effects on pulmonary circulation and RV function.

Four-dimensional (4D) flow MRI [4] is a non-invasive technique for analyzing hemodynamic changes and correlating flow alterations in the pulmonary vasculature [5, 6]. 4D Flow MRI allows for the visualization of multidirectional flow features and alterations in these features associated with cardiovascular diseases. It has enabled more comprehensive access to pulsatile blood flow through the cavities of the heart and great vessels, with typical spatial resolution of  $(1.5 \times 1.5 \times 1.5)mm^3$  -  $(3 \times 3 \times 3)mm^3$ , typical temporal resolution of 30-40 ms, and acquisition times in the order of 5 to 25 min [7]. Computational fluid dynamics tools can be used to access the hemodynamic environment in the pulmonary arteries of diseased subjects and can help understand hemodynamic changes that are induced by geometric modifications and abnormal flow rates. A combined MRI and computational fluid dynamics (CFD) approach [8, 9] can be used to construct subject-specific pulmonary artery models and correlate flow alterations in ARDS. This non-invasive technique can further facilitate the bench-bedside approach in dealing with patients while weaning from mechanical ventilation. It is of prime importance to come up with mechanical weaning parameters that can predict weaning success and include cardiovascular reserves in their determination.

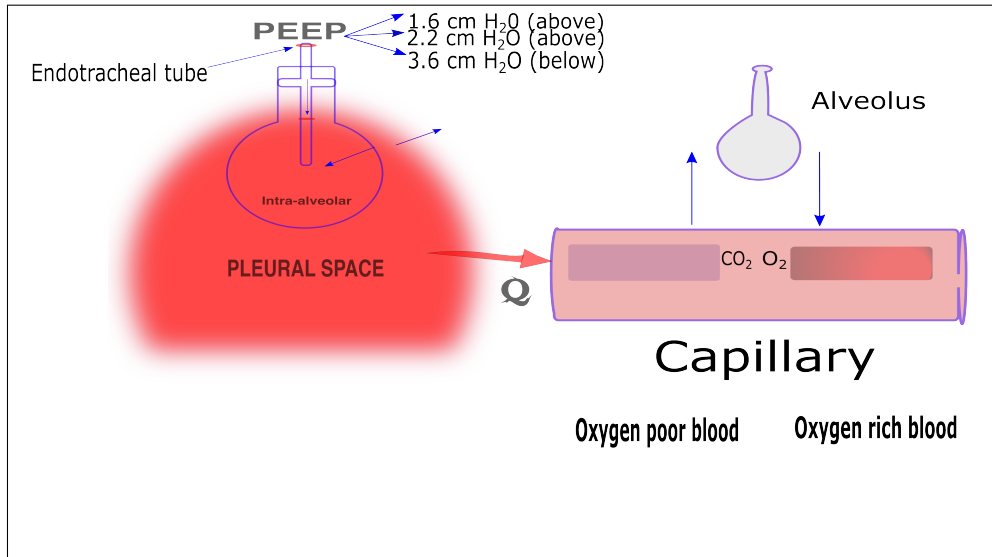


**Fig. 1:** Schematic diagram demonstrating blood filled capillary absorbing oxygen from inflated alveolus and leaving behind carbon dioxide. Respiratory system gets interrupted by ARDS and mechanical ventilation assists in bypassing constricted airways and deliver highly oxygenated air to help damaged lungs diffuse more oxygen. PEEP value used in the experiment is with respect to the highest compliance level.

## 2 Overview

### 2.1 Contribution

We demonstrate how to facilitate the bench to bedside approach and assist pulmonologists in understanding the role of mechanical ventilation in the treatment and control of collateral damage of lungs by the subject-specific modeling. This is the first CFD study of ARDS cases correlating the ventilation modes and cardiovascular risks. The contributions of our study to the existing literature on the hemodynamics of ARDS cases are as follows:

- Qualitative validations of the CFD simulations for subject-specific flow rate at the inlet and Windkessel (RCR) boundary conditions at the outlet with in-vivo experiments to correlate the flow alteration in the main pulmonary artery (PA) for experimental ARDS cases.
- Numerical comparison of the quantitative parameters for different spectra of ARDS conditions. We examined various hemodynamic parameters such as time averaged wall shear stress (TAWSS), and oscillatory shear at the lower curvature arc of porcine PA where flow alterations were observed.
- We examined the effects of mechanical ventilation induced changes on hemodynamic variables and determined whether these findings are robust and occur under different geometries, heart rates, and flow conditions. We also investigated whether ventilation induced hemodynamic changes can lead to self amplification of flow-induced progressive vascular dysfunction and its consequences on the right ventricle (RV).

### 2.2 Outline

This paper is organized as follows: In Section 3 we present the methodology related to data acquisition, the approach to segmentation of the pulmonary artery and mesh generation. In Section 4, we present the blood flow model along with boundary conditions. It is important to mention that the rigid wall model is used here, which should be sufficient to reproduce all spectra of experimental ARDS condition. The rigid model is an appropriate model that has been verified in the literature for disease cases [10]. In Section 5, we show the convergence results, periodicity reached during the cardiac cycles, and validation of our numerical simulations with the in-vivo experiment. We also present the comprehensive study of flow impingement sites that occurs in main pulmonary artery for different spectrum of ARDS and propose a potential flow induced biomarker for distinguishing between different ventilated condition. Finally in Section 6 and 7, we discuss the limitation and perspective of our contribution in relation to pulmonary vascular dysfunction and mechanical ventilation.

### 3 Methodology: Data acquisitions and Mesh Generation

#### 3.1 Data Acquisition

##### 3.1.1 Animal Model

Data were collected at the Spanish National Center for Cardiovascular Research, CNIC, Spain and the animal study was approved by the Institutional Animal Care and Use Committee and local authorities. *"sus scrofa domesticus"*, large white breed pigs ( $37 \pm 6.5$  kg) were used in this study. Saline ( $30ml/kg$ ) lung lavages were performed until  $PaO_2/FiO_2 < 300$  mmHg at  $5cmH_2O$  PEEP and  $1.0 FiO_2$  was reached. Thereafter, three positive end-expiratory pressure levels were applied in random order: hyperinflation,  $6\text{ cm } H_2O$  above; open lung approach,  $2\text{ cm } H_2O$  above; and collapse,  $6\text{ cm } H_2O$  below the highest compliance level [11] .

##### 3.1.2 MRI Data

A comprehensive cardiovascular magnetic resonance (CMR) examination was conducted utilizing a 3.0-Tesla magnet (Achieva-Tx, Philips Medical Systems, Best, the Netherlands) equipped with a 32-channel cardiac phased-array surface coil and employing retrospective electrocardiographic gating. Concurrent monitoring of pulmonary artery (PA) and systemic pressures was carried out using a CMR-compatible monitor (Invivo, Orlando, Florida).

For cine imaging, steady-state free precession cine sequences were acquired in 10 to 15 contiguous short-axis slices spanning both ventricles from base to apex. These images were subsequently reconstructed into 25 cardiac phases, enabling the assessment of ventricular volumes and function. Two-dimensional flow imaging (phase-contrast) was also performed perpendicular to the main pulmonary artery, utilizing a velocity-encoded gradient echo sequence with the minimum upper velocity limit to prevent signal aliasing. The following parameters were employed for 2D flow imaging: repetition time/echo time of  $5.4/3.4$  milliseconds, a number of averages set at 2, slice thickness of 8 millimeters, voxel size of  $2.5 \times 2.5$  millimeters, and 40 reconstructed heart phases.

The CMR study incorporated the measurement of blood flow velocities, providing complete volumetric coverage of the pulmonary artery using a 4D flow MRI pulse sequence. The specific imaging parameters for this sequence included a 10-degree flip angle, echo time/repetition time of  $2.3/3.9$  milliseconds, a field of view measuring  $(280 \times 280 \times 98)mm^3$ , an acquired resolution of  $(0.875 \times 0.875 \times 0.098)mm^3$  reconstructed to  $(0.875 \times 0.875 \times 0.098)mm^3$ . Three velocity-encoding directions were applied: foot-to-head (FH), left-to-right (LR), and anterior-to-posterior (AP), with a temporal resolution set at a velocity encoding of 200 centimeters per second. The 3D images were acquired with a SENSE factor of 2.56 in the anterior-to-posterior direction. The total acquisition time was 542 seconds.

To obtain the MRI data for different spectrum of ARDS condition, the pulmonary surfactant of the animal was removed so that the animal gets sick and needs to be mechanically ventilated, similar to patients in the Intensive Care Unit. Due to removal

of surfactant, surface tension goes up making it harder for the lungs to ventilate and utilize for gas exchange, which may possibly cause hypoxemia. To get the final ARDS status, animals were mechanically ventilated for two hours at total lung capacity, which leads to well-known acute lung injury and it induces pulmonary edema. For each subject, images were acquired under several conditions: 1) Baseline, and 2) after inducing acute respiratory distress syndrome, under three different positive end-expiratory pressure conditions, which were selected randomly. These conditions included: a)Hyperinflation (HI) b)Open Lung Approach (OLA), and c) Collapse (COL). These different conditions vary in pressure values from the highest compliance level.

### 3.2 Deep Learning approach to PA segmentation:

In this study, an automatic pulmonary artery segmentation model is developed to enable the generation of input meshes for CFD simulations. 4D flow images of six pigs in different conditions, yielding 24 imaging studies, are employed to train and test the 3D Convolutional Neural Network proposed by [12] . For the segmentation model, the 3D velocity-encoded phase contrast MRI sequences are selected, as the PA can be easily identified. The velocity information from the three axes has been merged into a single three-channel image where each element represents a flow direction. Then, the modulus of the three channel image is calculated, obtaining a grayscale image where the pulmonary artery appears contrasted, as displayed in **Fig. 2**. In 13 of the studies, the PA has been manually segmented by experts, and automatically post-processed to correct small imperfections in the masks.

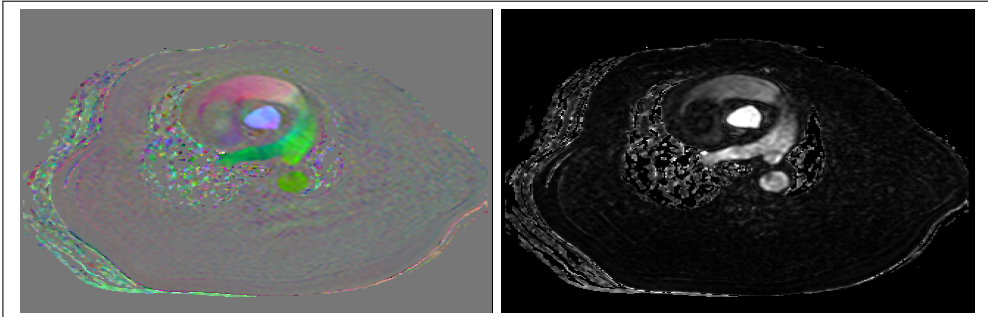


**Fig. 2:** (Left:) axial slice of a three-channel 3D velocity-encoded image (Right:) the same axial slice of the modulus of the three-channel 3D velocity-encode image

A cross validation has been performed employing the manual segmented studies, separating the 13 images in 4 groups. In each fold, the network has been trained during 50 epochs employing the Adam optimizer with a learning rate of 0.001 and a Weighted Dice loss function (a weight of 0.9 for the artery and 0.1 for the background). This has resulted in an average dice coefficient of  $0.795 \pm 0.034$  and Jaccard coefficient of

$0.665 \pm 0.043$  across the 4 folds. Here are some examples of the automatic segmentations (green color) superimposed to the manual segmentations (orange color):

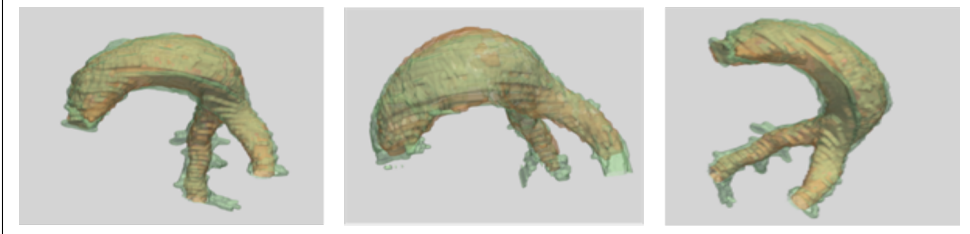


**Fig. 3:** Demonstration of the performance of the automatic segmentation. It is observed in all the three figures (Left, middle, and Right) that the automatic segmentation (Green) fits quite well with the ground truth (Orange).

### 3.3 Model Info and Grid Generation

The segmented image is used to create a solid model after a series of smoothing and remeshing steps. The centerline information was used to clip the geometries, followed by the creation of a surface and volumetric mesh. Isotropic meshing was implemented by specifying the maximum edge length and mesh density were increased locally at the faces to maintain quality and avoid self intersections. For clipping and mesh generation, we used open source software framework (OpenFlipper, Tetgen, and VMTK )[\[13–15\]](#). We want to emphasize that we did not adopt any adaptive meshing strategy.

## 4 In-Silico Model

### 4.1 Blood-Flow Model

To model blood flow in the pulmonary artery with one bifurcation, we consider the incompressible Navier-Stokes equations motion of a fluid in terms of its velocity, pressure, and density expressing conservation of momentum and incompressibility of a constant temperature Newtonian fluid, and constant kinematic viscosity. It is important to note that many factors can influence the accuracy of the simulation, such as the accuracy of the model geometry and assumptions made in the simulation. The external body force representing gravity was neglected and the vessel wall boundary is assumed to be rigid for all test cases. Further details of the blood flow model are mentioned in the Appendix A. Once we set up the equations and tune the model with appropriate parameters, we need to specify the boundary conditions.

#### 4.1.1 Inflow boundary condition

The inflow boundary conditions are typically imposed as velocity profiles (parabolic, plug and Womersley) on the inlet face. For our simulations, subject specific pulsatile flow rate was prescribed at the inlet assigning parabolic profile for the flow (**Fig. 4**).

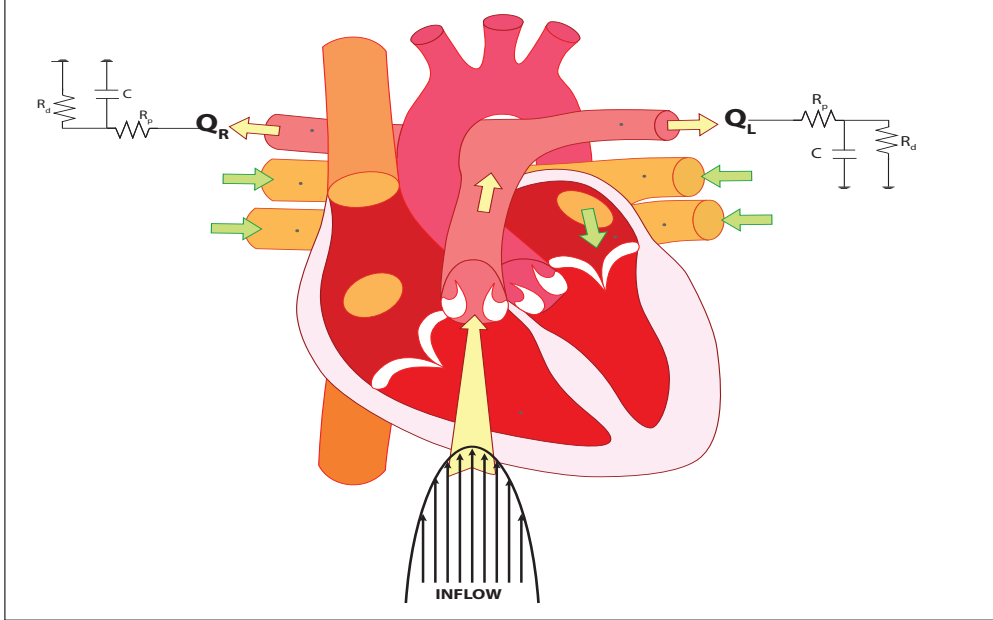


**Fig. 4:** In-silico model of the blood flow with parabolic flow waveform prescribed at the inlet and 3-element(RCR) windkessel model at the outlet. Figure modified from Wikimedia Commons.

Depending on specific artery under investigation, the flow rate can typically vary. We assigned flow rate near the RV. 4D PC-MRI data describe time resolved, 3D blood flow information of one heartbeat consisting of systole, and diastole. We used PC-MRI data to extract the subject specific pulsatile flow waveform. The temporal flow rate at the RV plane was mapped to inlet face by first interpolating with Fourier series and then by Schwartz-Christoff mapping [16]. The flow split at the outlet was calculated using Murrays law [17, 18].

#### 4.1.2 Outflow Boundary Condition

At the outlet the Navier-Stokes are coupled to a reduced order model which takes into account the rest of the vessel. To replicate the impact of vessels distal to CFD model branches, a three-element Windkessel model was imposed using a coupled-multidomain method [19]. This method represents arterial networks using three parameters with physiologic meaning: proximal resistance ( $R_p$ ), capacitance (C), and distal resistance ( $R_d$ ) (Fig. 4). Compliant arteries accumulate blood volume pumped in systole and release this volume during the diastole causing a continuous peripheral blood flow during the entire cycle. The Windkessel effect thus refers to the transient storage of both blood and mechanical potential energy in the large arteries during systole, which is then released during diastole. The total arterial capacitance (TAC) for each patient was determined from pleural pressure and stroke volume. This data was provided by the experimentalists. The TAC was then distributed among outlets according to

their blood flow distributions[17, 18]. Once the capacitance term for each branch was assigned, the total resistance ( $R_T$ ) of the vasculature ( $R_T = R_p + R_d$ ) was calculated from mean blood pressure ( $P_{mean}$ ), Pulmonary arterial wedge pressure (PAWP) and mean flow rate ( $Q_{mean}$ ) using equation (1). We want to mention that the equation (1) used for calculating pulmonary vascular resistance is different from the expressions used in systemic circulations.

$$R_T = PVR = \frac{(P_{mean} - PAWP)}{Q_{mean}} \quad (4.1)$$

For pulmonary vascular resistance, it is necessary to use not only the mean artery pressure but also the outflow pressure which in pulmonary circulation is the left atrium mean pressure and equals the wedge pressure (PAWP). The outflow pressure cannot be assumed to be zero for pulmonary circulations. In multi-coupling approach where we have a 3D-fluid domain coupled with a 0D domain, there is often a problem of divergence at the outlet boundary. The most common idea is to use 3D-0D coupling where we enforce a uniform normal stress at the outlet which equals the pressure given by the reduced model. In a finite element framework this is performed with the neumann boundary conditions as mentioned in Appendix A.

## 4.2 Simulation setting

Once all the boundary conditions were applied, the flow solution for each subject-specific mesh was obtained using a stabilized finite element method realized in svSolver [16] to solve the incompressible Navier-Stokes equations. The number of mesh nodes needed to achieve the computations varies from baseline to ARDS and from one ventilated case to another. The maximal number of mesh nodes generated for the simulation was  $11 \times 10^6$ . The computations generally approximately one day utilizing 48 cores and without considering the pre-processing (format conversion, smoothing etc.). For validations, we chose time-steps in accordance with the CFL condition and also the time frame of MRI images. Let us denote the simulation time chosen in accordance with CFL condition as  $\Delta t$  and the time frame of MRI acquisition as  $\Delta T$ , then the number of restart files chosen to save simulation is  $\lceil \frac{\Delta T}{\Delta t} \rceil$ , where  $\lceil \rceil$  is a ceiling function. The number of time-step required for the simulation were chosen to be  $\lceil n \frac{T}{\Delta t} \rceil$ , where  $T$  is the cardiac cycle obtained from experiments, and  $n$  is the number of cardiac cycles. The simulations were conducted over six cardiac cycles, and the final visualizations of the last few cycles were meticulously recorded. It should be noted that if the initial pressure and velocity conditions were set to zero, the flow would reach full development within the six cycles. Proof supporting this conclusion can be found in the Appendix B. To preserve the physiological periodicity of the blood flow in animals, the inlet flow was interpolated using a Fourier series choosing one simulation cycle as one cardiac cycle. Backflow stabilization with a stabilization coefficient value of 0.2 was introduced to mitigate the impact of simulation instabilities. It prevents outflow divergence and maintains a physiologically accurate blood flow in the baseline, diseased and ventilated cases. In addition, we have the

following simulation settings (**Tables 1** and **2**) in this study:

- Physiological assumptions

**Table 1:** Blood physiological parameters (millimetre,gram,second) unit).  
 Blood density:  $(\frac{g}{mm^3})$ , Blood viscosity:  $(\frac{g}{(mm.s)})$

Conditions	Wall-model	Blood Viscosity	Blood density
Baseline	Rigid	0.004 g/(mm.s)	0.00106 g/mm <sup>3</sup>
Ventilated(COL, HI, and OLA) ARDS	"	"	"
	"	"	"

- Parameters selection

**Table 2:** Simulation parameters (mgs unit) used for different ventilatory condition.  
 Capacitance:  $(\frac{mm^5}{dyne})$ , PVR:  $(\frac{dyne.s}{mm^5})$

Subject	$\Delta t$ (Simulation)	PVR(Pulmonary vascular Resistance)	Cardiac-cycle	Capacitance
2327(B)	0.0040s	0.0056	0.858s	189.76
	0.0029s	0.0096	0.485s	98.95
	0.0036s	0.0184	0.573s	85.90
	0.0032s	0.0113	0.450s	49.80
	0.0031s	0.0139	0.593s	60.17
2444(B)	0.0025s	0.0049	0.585s	189.02
	0.0045s	0.0015	0.734s	150.001
	0.0029s	0.0050	0.582s	68.084
	0.0029s	0.0098	0.427s	92.25
	0.0030s	0.0015	0.453s	81.02
2459(B)	0.0024s	0.0060	0.781s	181.04
	0.0030s	0.0059	0.451s	186.27
	0.0020s	0.0045	0.472s	239.46
	0.0032s	0.0119	0.481s	60.35
	0.0020s	0.0053	0.457s	125.60
2672(B)	0.00345s	0.0041	0.844s	310.531
	0.0035s	0.0029	0.571s	296.905
	0.0025s	0.0048	0.474s	646.51
	0.0030s	0.0037	0.390s	228.410
	0.0029s	0.0054	0.477s	159.5240

## 5 Numerical results

A GMRES solver with 100 Krylov vectors per GMRES sweep was used to solve the discretized system of equations. To validate the in-silico experiment for different physical parameter we tune the proximal and distal resistance by varying the values of  $\kappa$  in the equation  $R_p = \kappa R_d$ , where  $\kappa \in \{0.10, 0.20, 0.30, 0.40, 0.50\}$ . As we increase the value of  $\kappa$  from 0.10 to 0.50, the stabilization method forces the solution to be fully developed in only a few cardiac cycles as shown in **Fig. 6**, and analyzed in Appendix B. The value of the characteristic fill time ( $C \times R_d$ ) is an important parameter in the analysis of blood flow and can be used to assess the behavior of the flow and pressure distribution within the vascular system. When a high value of the ratio ( $\kappa$ ) was selected, the resulting characteristic fill time was high, indicating the presence of a high-frequency flow pattern. Consequently, the pressure values were amplified and did not match the in-vivo experiments. This implies that the flow rapidly fills the vessel, leading to high pressure within it. It is important to emphasize that pulsatile RCR has a characteristic fill time, which represents how the distal vasculature stores and releases the flow. We observed that the simulations matched the in-vivo experiment for a value of  $\kappa = 0.10$ . For our simulations, we chose  $\frac{R_p}{R_d} = 0.1$  in defining the metrics for the identification of biomarkers.

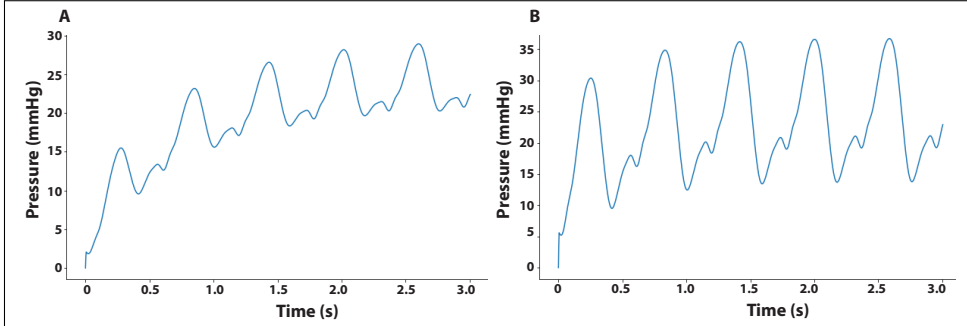


**Fig. 5:** Effect of tuning parameter ratio  $\kappa$  : A)  $\kappa = 0.10$  and B)  $\kappa = 0.50$  on the pressure signals at the outlet.

### 5.1 Verification and validation:

In **Fig. 6**, we verify the convergence properties of our numerical simulations by looking at the average residual error ( $\frac{\|Res\|}{\sqrt{No.ofnodes}}$ ) for the last non-linear iteration. It is clear from the results that the numerical simulations achieved the desired tolerance, which was set to  $10^{-4}$  for all cases. Additionally, it is apparent that the flow is fully developed as indicated by the periodic behavior observed in the pressure curves at

the outlet face (**Fig. 6C**). The pressure curves exhibit a repeating pattern, indicating that the flow has reached a steady state and is no longer influenced by the initial conditions. This periodic behavior is a strong indication of a fully developed flow and demonstrates that the simulations accurately captured the behavior of the system. It is also important to validate the simulation results against a sufficient number of in-vivo measurements to ensure that the simulation is accurately predict the behaviour of the blood flow in the pulmonary artery. To meet this requirement, we matched the systolic, diastolic and mean pressure values obtained from the simulation to the corresponding in-vivo reported values. The pressure values reported matched with the in-vivo systolic pressure but there was significant deviations in the diastolic pressure from the in-vivo results. The mismatch is primarily attributed to the fact that, during ventricular diastole smaller arteries(branches) and arterioles serve as the chief resistance vessels and we only ran simulations for Main Pulmonary Artery (MPA) along with initial bifurcation of the left and right pulmonary artery (LPA and RPA, respectively). We validated the temporal evolution of the average velocity values in the slice before bifurcation (**Fig. 7**). The choice of the plane before bifurcation was made to prevent the results from being influenced by the placement of the slices. By selecting this location, the procedure is less susceptible to errors that may be introduced by slicing the data at an inappropriate location. This helps ensure the accuracy and reliability of the results, and provides a better understanding of the behaviour of blood flow. The small deviation observed in the results is primarily attributed to the artifacts introduced by the segmentation process. Finally, in **Fig. 8**, we demonstrate the qualitative validations of our numerical simulations using the in-vivo results. We observed strong vorticity during the early diastolic phase and after the peak systole in the form of a hellicoid. The presence of a vortex was noticeable in the mid-plane of the MPA in cases where there was a small curvature. This phenomenon was observed in all the cases in which the disease was present. The visualization of vortices in the MPA in the regions above the low-curvature arc provides valuable insight into the behaviour of the blood flow and the effects of disease on flow dynamics.

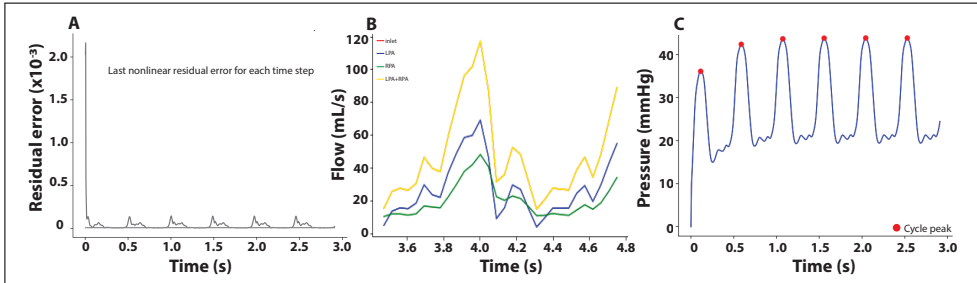


**Fig. 6:** Verification of the numerical convergence with tolerance  $10^{-4}$ . A) Residual error at the last non-linear iteration B) Visualization demonstrating conservation of flow rate in the last cycle of simulation C) Periodicity in pressure values at the outlet.

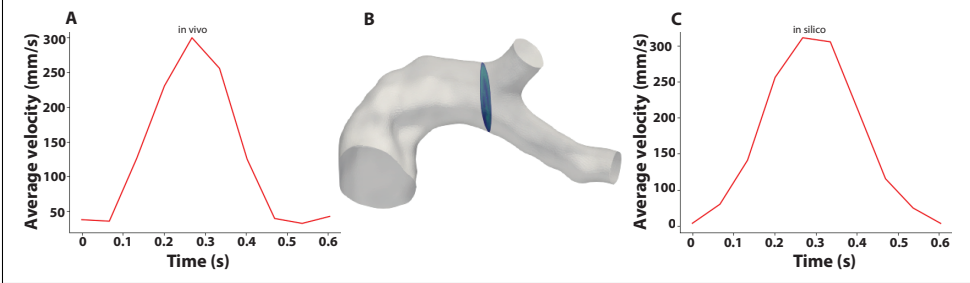


**Fig. 7:** Secondary validation: Matching velocity profiles: A) Space averaged temporal evolution of velocity values from in-vivo, B) demonstration of plane location at which the values were matched C) Space averaged temporal evolution of velocity values from in-silico simulation for one subject.

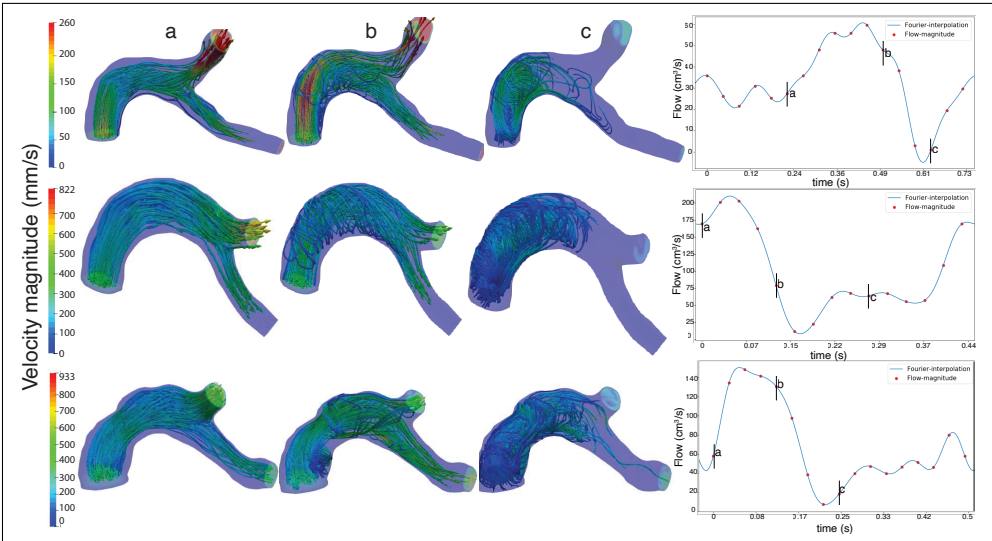


**Fig. 8:** Velocity streamlines for different subject during a) acceleration phase b) deceleration phase and c) early-diastolic phase of the cardiac cycle

### 5.1.1 Flow Impingement Sites:

Flow impingement velocities occur when channels direct flow into a bank line at large acute angles, resulting in flow concentration along the bank lines. We have a similar situation in cases of the pulmonary artery with MPA, LPA and RPA. Flow impingement can also occur when abrupt changes occur in the geometry of the artery, such as sudden expansions or contractions. This can cause the flow to separate from the walls of the vessel, leading to an increase in wall shear stress and potentially damaging the arterial endothelium. These flow impingement velocities create large forces on the arterial wall and increase blood residence time. In **Fig. 8**, we can observe that

Subject	Regurgitation Fraction	In-silico observation
2327(B)	0.0	No backflow
A	0.0	No Backflow
C	0.07	No Backflow
H	0.23	Backflow
O	0.0	No Backflow
2444(B)	0.93	Severe Backflow
A	0.0	No Backflow
C	0.02	No Backflow
H	0.16	Backflow
O	0.38	Backflow
2459(B)	0.04	No Backflow
A	0.01	No Backflow
C	0.0	No backflow
H	0.0	No backflow
O	0.0	No backflow
2672(B)	0.0	No backflow
A	0.0	No backflow
C	0.0	No backflow
H	0.0	No backflow
O	0.0	No backflow
2487(B)	0.0	No backflow
A	0.0	No-backflow

**Table 3:** Quantification of Regurgitation fraction in different subjects.

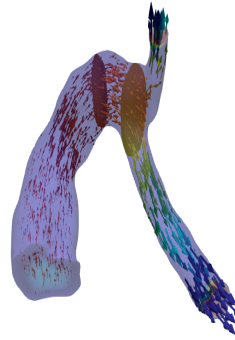


**Fig. 9:** Landmarks:above the Pulmonary Valve(proximal), above minimum curvature arc(med), before bifurcation(distal), beginning of the LPA(L) and beginning of RPA(R)

regions of low curvature are the flow impingement sites where helicoidal patterns can be observed in the flow during early diastole and after the peak systole.

### 5.1.2 Landmark measuring planes and analysis.

For our analysis, five landmarks (positions on the vessel centerline [20]) were investigated. 1) Above the pulmonary valve, 2) above the minimum curvature arc, 3) before the bifurcation, 4) beginning of the left pulmonary artery, 5) beginning of the right pulmonary artery. All measuring planes that were specified as landmarks (proximal, mid-slice, and distal ) (**Fig. 9**) were pre-evaluated for various statistics such as velocity, helicity, and wall shear stress (mean, max, and median). Finally we plotted the correlation heat map (**Fig. 10**) of different bio-markers (vorticity (w), helicity (h), and wall shear stress (wss)) indicating their significant correlations. We found that the biomarkers associated with shear stresses at flow impingement sites (mid-slice, proximal, and distal) have better correlations with the helicity which is a measure of vorticity. The metrics incorporating wss can be potential non-invasive biomarkers that correlates mechanical ventilation and cardiovascular risks which may further predict weaning success.

### 5.1.3 Backflow and quantification of pulmonary regurgitation

We tested for the presence of pulmonary regurgitation (**Table 3**): a pathology in which the pulmonary valve does not close completely and can sometimes lead to valve replacement surgery if the symptom is severe. We considered the flow rate conservation with the implemented numerical schemes by measuring the volume of liquid entering the main trunk and volume of liquid exiting from the left and right pulmonary branches during the entire cardiac cycle. The time dependent flow rate  $Q(t)$ ,  $t \in [0, T-1]$ , where  $T$  is the number of temporal positions in the dataset, is required to calculate the stroke volume of the plane P. Since a 4D PC-MRI dataset contains one full heartbeat,  $Q(t)$  is

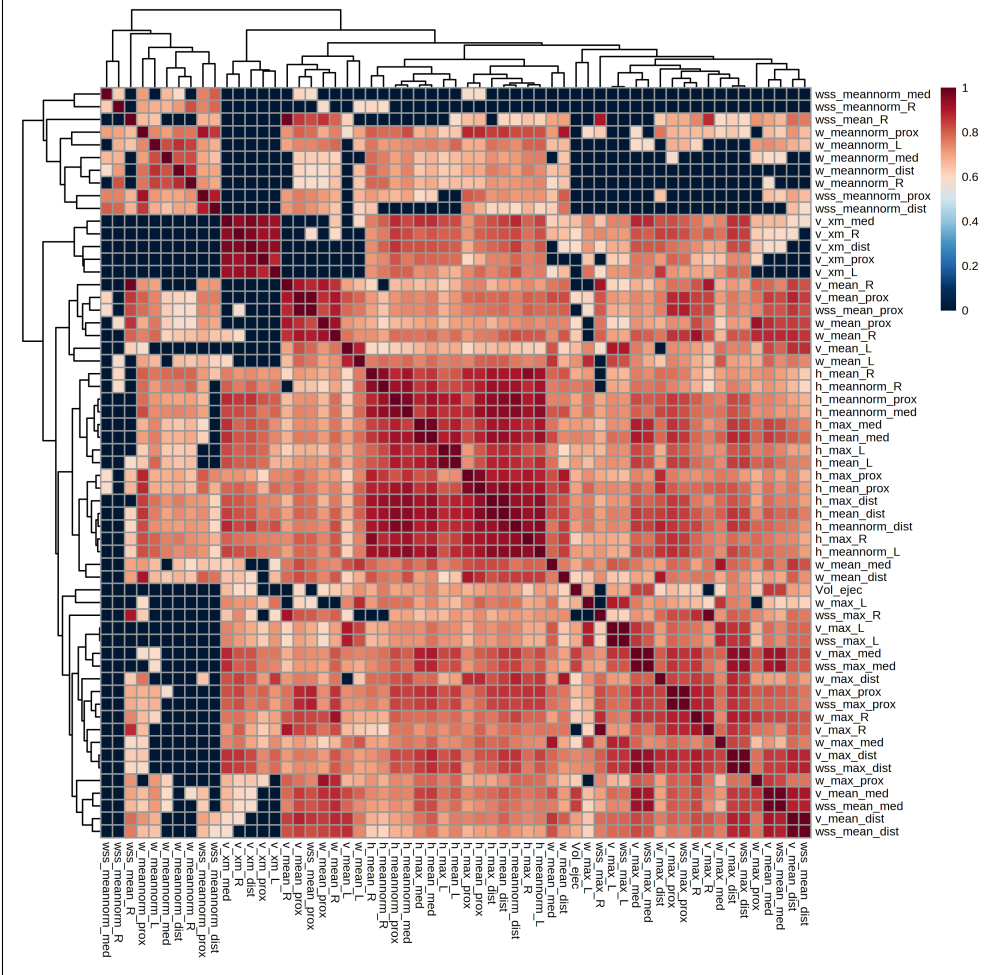


**Fig. 10:** Analysis of different features extracted on the landmark measuring planes (proximal(prox), mid-slice(med), distal(dist), L, and R) and their correlations. h\_mean\_med denotes average helicity at the mid-slice, wss\_max\_med denotes maximum wss at the mid-slice and similarly other features have been indicated with respect to the slice positions (L, R represent the beginning of left and right pulmonary artery respectively).

periodic. The integral of  $Q(t)$  gives the stroke volume. We calculate the time-dependent flow rate at the inlet, and integrate over the cardiac cycle to get retrograde volume ( $rV$ ) and antegrade volume ( $aV$ ). The regurgitation fraction ( $RF = \frac{aV}{aV+rV}$ ) was calculated to assess the presence of backflow. The regurgitation fraction represents the fraction of the blood that flows backwards in the direction opposite to the normal flow. In this study, a threshold of 0.05 was chosen as the criteria for the emergence of backflow. By using the regurgitation fraction and this threshold, it is possible to determine the

presence of backflow (**Table 3**) and to understand its impact on the flow dynamics. Anomalous behavior was noted in subject 2444 during the baseline condition of the experiment. This unexpected behavior may be attributed to the animal's prior illness before the start of the experimental procedure and also to the peculiar physiology of swine pulmonary vascular system. Furthermore, it is important to acknowledge that pigs possess inherent capabilities for exhibiting backflow behavior and are prone to hypoxic vasoconstriction.

## 5.2 Metrics for analysis and potential predictor:

Additional mechanical information like fluid dynamics, the study of forces and stresses are important in mechanical ventilation. Mechanical ventilation alters flow behaviour (**Fig. 8**) in the main pulmonary artery and the flow exerts mechanical forces on the vessel wall eliciting cell mediated biological pathways. This can cause disturbed blood flow and lead to increased shear forces on the vessel walls, which can damage the arterial endothelium. Time Averaged Wall Shear Stress (TAWSS) and Oscillatory Shear Index (OSI) [21–23] play pivotal role in studying the mechanobiological stresses of endothelial cells. In this study we aimed to analyse the mechanical trauma on the blood element under different ventilatory maneuvers. The TAWSS at an arbitrary position  $x$  is the average magnitude of the wall shear stress vector  $\tau_w$  over one cardiac cycle of duration  $T$  at that point.

$$TAWSS(x) = \frac{1}{T} \int_0^T \|\tau_w(x, t)\| dt$$

The oscillatory shear index quantifies the change in the orientation of the wall shear stress vector during a cardiac cycle and is calculated as

$$OSI(x) = \frac{1}{2} \left( 1 - \frac{TAWSSV}{TAWSS} \right)$$

Using TAWSS and TAWSSV ( $\frac{1}{T} \|\int_0^T \tau_w(x, t) dt\|$ ), OSI clarifies the wall shear stress vector deflection from blood flow predominant direction during cardiac cycle. The OSI value can vary from 0.0 for no cyclic variation of wss vector, to 0.5 for 180 degree deflection of wss direction. We visualize TAWSS (**Fig. 11 A, C, E,G**) and OSI (**Fig. 11 B, D, F, H**) for one subject in all the condition at the flow impingement sites. We observe low TAWSS values (depicted in blue) in the MPA. These are the areas where the average shear forces are relatively low. These regions have reduced mechanical stimulation and might be at the risk of endothelial dysfunction. We observe relatively high TAWSS values in LPA and RPA which indicates that the vessel wall is experiencing relatively high average shear forces. These regions might be where endothelium is well stimulated. Furthermore, the assessment of OSI values in the MPA artery revealed regions exhibiting significant changes in flow direction, denoted by high OSI values. In contrast, areas downstream of the bifurcation displayed low OSI values, signifying consistent and unidirectional flow patterns. These observations have

served as a catalyst for the development of metrics that incorporate both TAWSS and OSI into their calculations. Such metrics hold promise for a more comprehensive evaluation of ARDS severity.

We propose two interesting metrics, Mechanobiological Score (MS)(2), and Mechanobiological index MI(3) which combine TAWSS and OSI as

$$MS(x) = \frac{2(OSI(x) \cdot TAWSS(x))}{OSI(x) + TAWSS(x)} \quad (5.1)$$

$$MI(x) = \frac{OSI(x)}{TAWSS(x)} \quad (5.2)$$

MS (**Fig. 12B**) always favors a lower value from TAWSS and OSI and is analogous to OSI (**Fig. 12A**) in our simulations as shown in **Fig. 12** for one subject. MS can be used as a primary confirmation of regions with disturbed and oscillatory flow patterns as it balances the lower values from both TAWSS and OSI as commented in Appendix C. However, the various ventilatory conditions could not be distinguished. MI is mainly used to characterize flow impingement at the arterial walls in the main pulmonary artery (MPA). A large value of MI signals a low TAWSS together with a high OSI. All the aforementioned quantities are used to quantify the flow environment and flow-induced shear stress experienced by endothelium. This predictor has the potential to impact the field of vascular remodeling and management of ARDS by controlling flow changes as a means to minimize mechanobiological stresses. To quantify the effect of mechanical ventilation on flow-induced biomarkers, we analyzed the relative changes in MI with different ventilation maneuvers. For this purpose, we constructed an average geometry out of all the ventilated condition and with the same number of nodes and triangular elements. The simulation was run for the corresponding ventilatory conditions and then the above mentioned metrics were calculated and averaged over the cardiac cycles. Using these metrics, we now define ARDS severity ratio (ASR) which represents the relative error between the baseline and ventilated maneuver. Given a time-averaged quantity  $\phi(x) = MI(x)$  at point  $x$ , the relative percentage change in  $\phi(x)$  (the baseline) and the ventilation mode ( $\phi^{vm}(x)$ ) is defined as

$$ASR = \frac{\phi(x) - \phi^{vm}(x)}{\phi(x)} \times 100 \quad (5.3)$$

We visualize the ASR in the average geometry of the two subjects with  $\phi(x)$  as baseline in (**Fig. 13**). We observed that positive end expiratory pressure consistent with OLA (Optimal Lung approach) has the minimum ASR value at the flow impingement site and the maximum value of ASR is around 20 percent (**Fig. 13E**) in one subject and around 40 percent (**Fig. 13C**) in another subject. Further visualizations and small proofs are presented in the Appendix. Simulations files can be found on the github page<sup>1</sup>.

---

<sup>1</sup><https://github.com/ellipsis14/4DFlow>

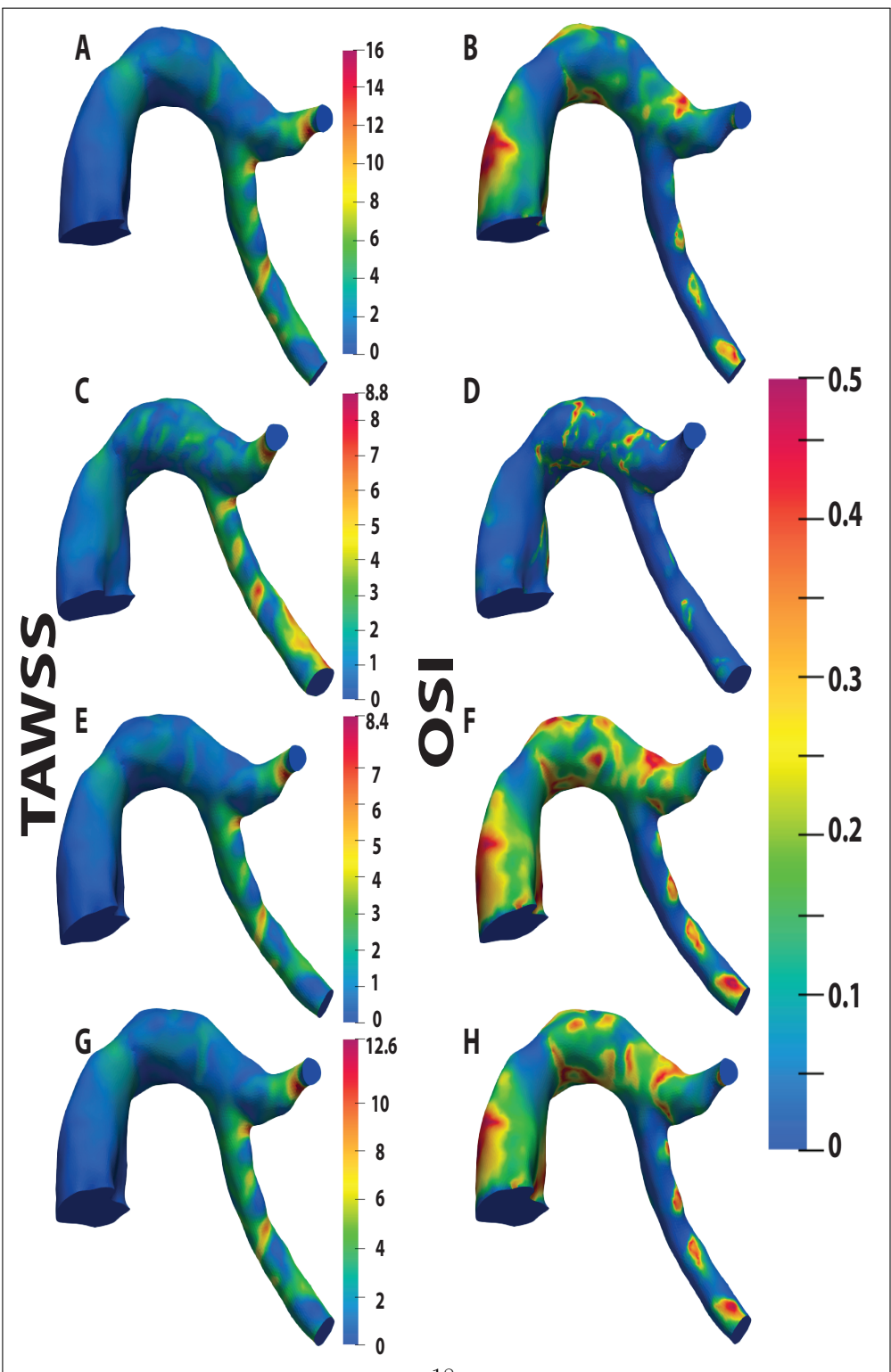


**Fig. 11:** Visualization of TAWSS( $\frac{\text{dyne}}{\text{mm}^2}$ )(Left) and OSI(Right) baseline for Subject 2459: Observation of high OSI at the sites of low TAWSS and viceversa.

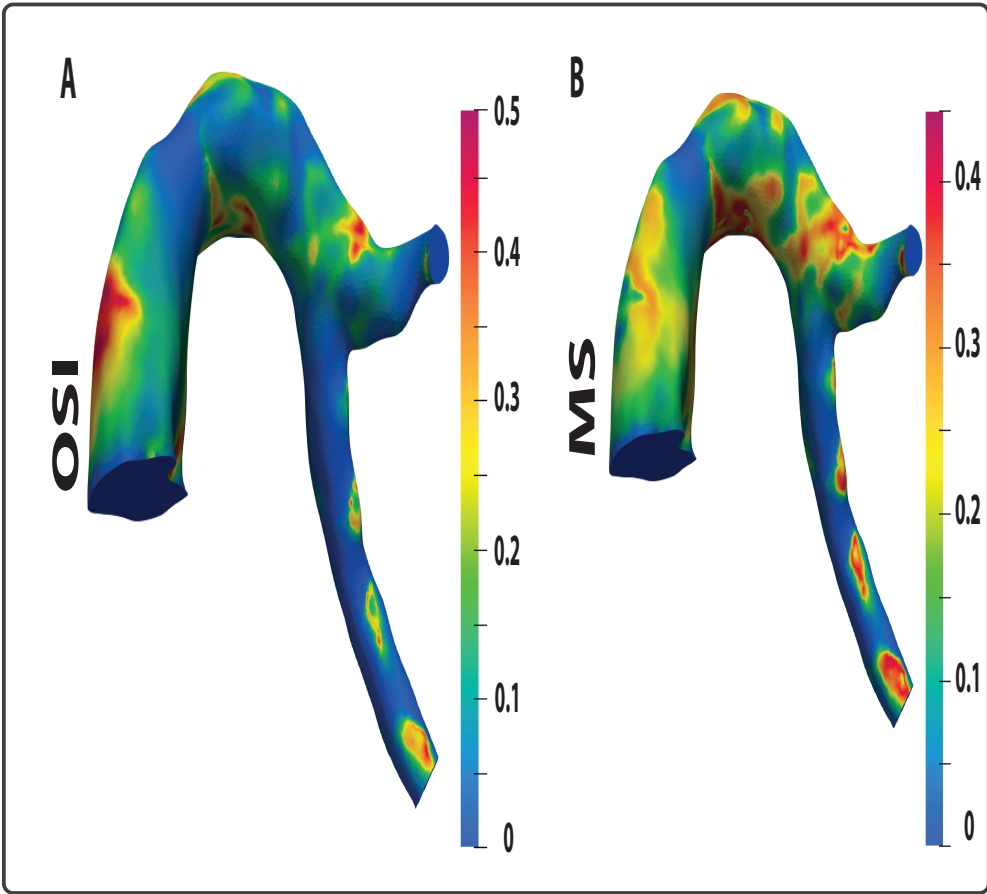


**Fig. 12:** Visualization of OSI and MS for subject 2459 in the baseline condition.

## 6 Limitations

The predictor we propose has been explored after processing the data from the experimental ARDS model with all its inherent limitations [11]. In addition, CFD simulations and post processing are computationally expensive. The computation time can be reduced using adaptive refinement guided by error control and robust post-processing of 4D-flow MRI. Although we performed an in depth analysis of the effect on flow in the pulmonary artery due to varied ventilation conditions, we only studied six animals under five experimental conditions.

Some segmentation artifacts were produced during automatic segmentation which in turn affected the performance of the CFD simulations. We made our best effort to control the factors affecting the segmentation and implemented further smoothing and refinements to maintain the aspect ratio quality of the mesh.

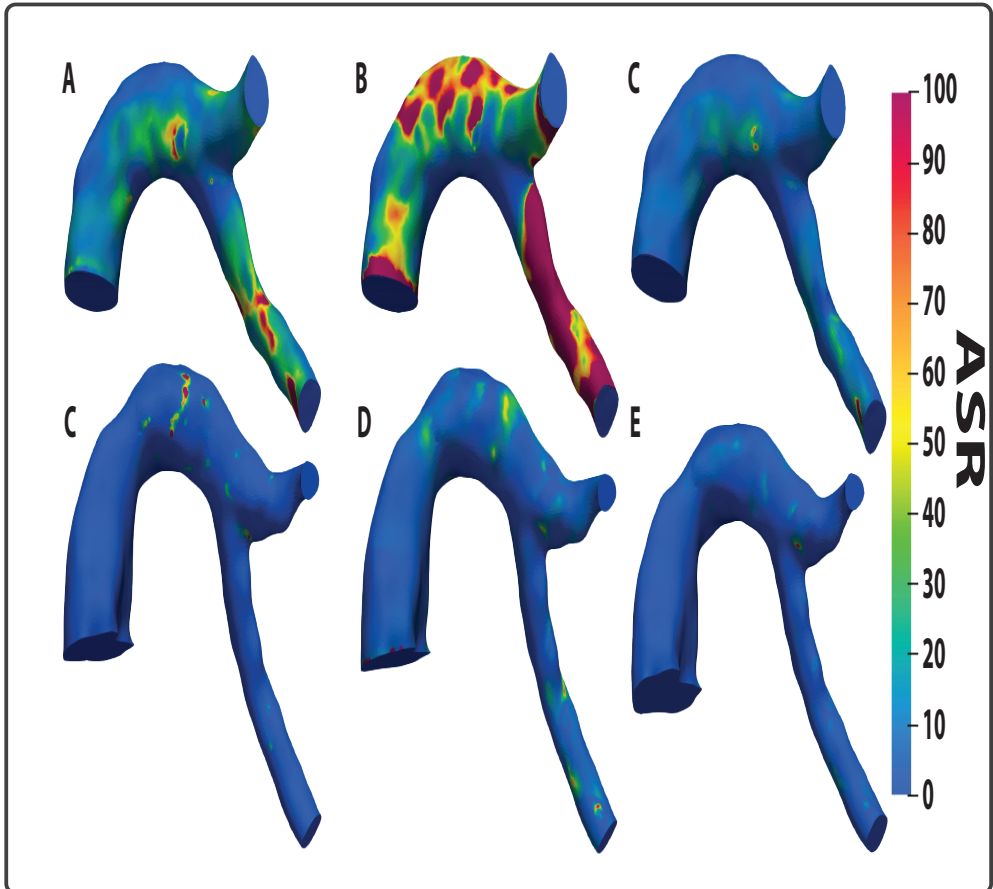


**Fig. 13:** ARDS severity ratio (ASR) of baseline with COL (Left)(PEEP:6cm  $H_2O$  above the highest compliance level) respectively.), HI (Middle)(PEEP:6cm  $H_2O$  below the highest compliance level) and OLA (Right)(PEEP:2cm  $H_2O$  above the highest compliance level)

The boundary conditions prescribed at the outlets come from the approximations of solutions of ordinary differential equations and are not a real pressure waveform extracted from in-vivo data. Nevertheless, we found clear distinction in the predictor values under various ventilatory conditions.

The subjects need to be transferred to the MRI unit to analyze biomarkers which limits its use in high-risk emergency situations and can only provide therapeutic interventions and guide medical decision making and treatment in low risk emergency conditions.

## 7 Conclusions and Perspectives

Simulations of Newtonian blood flow in different spectrum of ARDS conditions at realistic flow rates were performed, using a parallel scientific computation library. In particular, different ventilated conditions have been studied, and we noticed formation of helicoidal flow structures in diseased animals at lower curvature arc of the main pulmonary artery and also in some baseline conditions. Every disease occurs at the cellular level and we need predictors that encompasses endothelial mechanobiology. We require personalized predictors which are mechanistically relevant in particular patient at the particular moment of time. When endothelial cells are exposed to low and oscillatory shear stresses, they can respond by producing reactive oxygen species[24] recruiting more inflammatory cells, upregulating vascular cell adhesion, molecules and cytokines in the vessel wall; and increasing endothelial permeability[25, 26]. This endothelial permeability affects gas exchange which in turn affects the transport of oxygen rich blood as sticky and leaky endothelium, in combination with an increase blood residence time facilitates leukocytes transmigration in to the walls. Leukocyte-mediated pulmonary inflammation is a key pathophysiological mechanism involved in acute ARDS. The predictor MI combining TAWSS and OSI is known to elicit the inflammatory response in the vascular endothelium [27].

Traditional screening of ARDS focused on alveolar centric predictors and the proportionality between gas volume and compliance was the deciding factor for deep hypoxemia related disorders. COVID-19 leads, in some cases, to pulmonary edema, characterized by the abnormal accumulation of fluid inside lungs, which restricts gas exchange in the alveoli and impacts lung compliance. Unfortunately since pandemic, there is no magic number and it has been difficult to answer questions like a) What value of PEEP is needed b) What kind of PEEP is needed and c) When to intubate the patient ?. Lung preventive ventilation strives to prevent over-distention, or stretch, of the aerated lungs, as this has been shown to disrupt the pulmonary endothelium and epithelium, resulting in lung inflammation, atelectasis, hypoxemia and the release of inflammatory mediators [28]. This novel predictor MI suggests using flow as a means to measure the ability of cells to respond to different PEEP and become activated, and can play a crucial role in deciding beneficial and detrimental effect of certain PEEP and management of ARDS.

Implementing our proposal poses practical challenges, and the task of transporting respiratory distress patients with in a hospital can be very demanding. This novel idea could have far-reaching implications in various areas including Intensive Care and management of ARDS cases, providing patients with high-quality ventilation all the way to the MRI suite. It holds great promise for future research and technical developments in portable (MRI + Ventilator) systems in revolutionizing the way medical care is delivered, particularly relevant in personalized or precision medicine.

## Declarations

### Conflict of Interest Statement

The authors declare that the research was conducted in the absence of any commercial or financial relationships that could be construed as a potential conflict of interest.

### Author Contributions

RK and JRC designed the details of the specific computational and analysis protocols including studies on patient-specific geometries. JRC performed the MRI data acquisitions. RK performed the CFD studies, analysis, and biomarkers identification and wrote the first and final draft. AGS and IR extracted the velocity profile of the 4D Flow MRI data. MJS generated the ground truth for training the deep-learning network. KL, and MS performed automatic segmentation of the pulmonary artery. Author thanks Dr. Arnoldo Santos and Dr. Fernando Suarez Sipmann for reading the manuscript. All the authors contributed equally to the reading and approval of the final version of the manuscript.

### Funding

This work was performed under the Maria de Maeztu Units of Excellence Programme Grant MDM-2017-0720 funded by MCIN/AEI/ 10.13039/501100011033. JRC is funded by MCIN/AEI/10.13039/501100011033 and by ERDF A way of making Europe or European Union or European Union NextGeneration EU/PRTR Science, (PID2021-123238OB-I00 and PDC2021-121696-I00). JRC received funding from La Caixa Foundation (Health Research Call 2020: HR20-00075) and Fundación contra la hipertensión pulmonar.

### Data Availability Statement

The datasets [GENERATED/ANALYZED] for this study can be found in the Github repository [<https://github.com/ellipsis14/4DFlow>].

### Appendix A Blood Flow Model

With the usual notations as in [29], we consider incompressible Navier-Stokes equations expressing conservation of momentum and incompressibility of a constant temperature Newtonian fluid, constant kinematic viscosity  $\nu > 0$  in space time domain  $(\Omega \times (I = (0, T)))$  with boundary  $\Gamma$ . The boundary  $\Gamma$  is such that  $\Gamma = \Gamma_i(\text{inlet}) + \Gamma_w(\text{Wall}) + \Gamma_o(\text{outlet})$ ;  $\Gamma_i \cap \Gamma_w \cap \Gamma_o = \Phi$ , where  $\Gamma_i$  represents an inlet boundary where a Dirichlet boundary condition is prescribed on the velocity field;  $\Gamma_w$  represents the vessel wall boundary and  $\Gamma_o$  represents all outflow boundaries where a Neumann condition is prescribed. A well-posed initial boundary value problem is defined by the following partial differential equation subject to suitable boundary and initial conditions,

$$\rho D_{u,t} \underline{\mathbf{u}} - \nabla \cdot \underline{T} = f \quad \text{in } \Omega \times I \quad (\text{A1})$$

$$\operatorname{div}(\underline{\mathbf{u}}) = 0 \quad \text{in } \Omega \times I \quad (\text{A2})$$

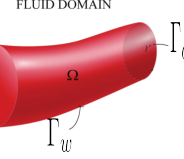
$$\underline{\mathbf{u}}(\underline{\mathbf{x}}, t) = u^{in}(\underline{\mathbf{x}}, t) \quad \underline{\mathbf{x}} \in \Gamma_i \quad (\text{A3})$$

$$\underline{\mathbf{u}}(\underline{\mathbf{x}}, t) = 0 \quad \underline{\mathbf{x}} \in \Gamma_w \quad (\text{A4})$$

$$\underline{T} = -pI + \nu(\nabla u + \nabla u^\dagger) \quad (\text{A5})$$

$$\underline{T} \cdot \underline{n} = \underline{h}(\underline{\mathbf{x}}, t) \quad \underline{\mathbf{x}} \in \Gamma_o \quad (\text{A6})$$

$$\underline{\mathbf{u}}(\underline{\mathbf{x}}, 0) = \underline{u}^0(\underline{\mathbf{x}}) \quad \underline{\mathbf{x}} \in \Omega \quad (\text{A7})$$



The external body force  $f$  representing gravity was neglected and the vessel wall boundary is assumed to be rigid for all test cases. Please note that  $\underline{h}$  in equation (A6) is the traction vector imposed on the outflow boundary. In order to define the variational form corresponding to the equations  $A_1 - A_6$ , we choose suitable trial and weighting function spaces. Considering this, the variational form for this problem can be written as:

$$a(\underline{w}, q, \underline{u}, p) = 0, \quad \text{where} \quad (\text{A8})$$

$$(\text{A9})$$

$$a(\underline{w}, q, \underline{u}, p) = \int_{\Omega} \underline{w} \cdot (\rho \frac{\partial \underline{u}}{\partial t} + \rho \underline{u} \cdot \nabla \underline{u}) + \nabla \underline{w} : (-pI + \sigma) d\underline{x} - \int_{\Omega} \nabla q \cdot \underline{u} d\underline{x} - \int_{\Gamma_o} \underline{w} \cdot (-pI + \sigma) \cdot \underline{n} ds + \int_{\Gamma} q \underline{u} \cdot \underline{n} ds$$

In the above expression  $\sigma = \nu(\nabla u + \nabla u^\dagger)$  is the stress tensor. The svSolver [16, 30] adopts Coupled-Multidomain formulation described in [10, 31]. The method is based on decomposition of domain  $\Omega$  into an upstream 3D numerical domain  $\hat{\Omega}$  and analytical domain  $\Omega'$  such that  $\hat{\Omega} \cap \Omega' = \Phi$  and  $\hat{\Omega} \cup \Omega' = \Omega$ .

## Appendix B Periodicity Proof

**Lemma B.1.** For  $\frac{R_p}{R_d} = \kappa$  and capacitance  $C$ , the characteristic fill time  $\tau = R_d C$  holds the relation

$$\tau < \frac{R_T}{\kappa} C \quad : R_T = R_p + R_d \quad (\text{B1})$$

*Proof.* This is obvious from the relation  $\frac{R_p}{R_d} = \kappa$ , which implies  $\frac{R_T}{R_d} = 1 + \kappa \implies \tau = R_d C < \frac{R_T}{\kappa} C$   $\square$

**Theorem 1.** For  $P(\vec{x}, 0) = P_0(x) = 0$ , the pressure step response of single RCR model, which is governed by the differential equation (B2) achieves periodicity in the number of cycles inversely proportional to  $\kappa$ , i.e two fold increase in  $\kappa$  shortens the time required to reach the periodic state by a factor of  $\frac{1}{2}$ .

$$P^{n+1} = \frac{P + \frac{\Delta t}{C} f(Q)}{1 + \frac{\Delta t}{C}} \quad (\text{B2})$$

where  $f(Q) = Q(1 + \frac{R_p}{R_d}) + R_p C \frac{dQ}{dt}$  (B3)

*Proof.* A three-element Windkessel model introduced in [32, 33] represented by equation (B2) and (B3) is used to describe the relationship between the blood flow and pressure at the outlet of arterial tree. Substituting (B3) in (B2), and taking the derivative in sense of limit, and rearranging the terms we observe the continuous form (B4).

$$\dot{P} + \frac{P}{\tau} = R_p \dot{Q} + \frac{1}{\tau} (R_p + R_d) Q \quad (\text{B4})$$

In view of [19, 34, 35], the mean pressure obtained from the semi-analytical solution of (B4) for a non-constant, periodic pulsatile inflow is given by

$$\bar{P}_n = \bar{P}_\infty + e^{\frac{-nT}{\tau}} [\bar{P}_0 - \bar{P}_\infty] \quad (\text{B5})$$

where  $\bar{P}_n = \frac{1}{T} \int_{nT}^{(n+1)T} P(t) dt$  is the mean pressure in the n-th cardiac cycle,  $\bar{P}_0$  is the initial mean pressure, and  $\lim_{n \rightarrow \infty} P_n(t) = \bar{P}_\infty$  is the asymptotic pressure. Starting at the  $\bar{P}_0$  and approaching the asymptotic mean pressure  $\bar{P}_\infty$ , equation (B5) can be rearranged as

$$\frac{\bar{P}_\infty - \bar{P}_n}{\bar{P}_\infty} = e^{\frac{-nT}{\tau}} \left(1 - \frac{\bar{P}_0}{\bar{P}_\infty}\right) \quad (\text{B6})$$

The left hand side of equation (B5) is the relative error between the asymptotic pressure and pressure in the nth cardiac cycle. Let's assume  $\frac{\bar{P}_\infty - \bar{P}_n}{\bar{P}_\infty} = \epsilon_\infty$ , and n as the number of cardiac cycles requires to reach the periodic state and taking logarithm to both side of (B6).

$$\begin{aligned} &\Rightarrow -\frac{nT}{\tau} + \ln \left(1 - \frac{\bar{P}_0}{\bar{P}_\infty}\right) = \ln(\epsilon_\infty) \\ &\Rightarrow -\frac{nT}{\tau} = \ln \left( \frac{\epsilon_\infty}{1 - \frac{\bar{P}_0}{\bar{P}_\infty}} \right) \end{aligned}$$

The left hand side is a positive integer and the right hand side is real number.

$$\Rightarrow n \leq -\frac{\tau}{T} \ln(\epsilon_\infty) \text{ for } \bar{P}_0 = 0$$

Substituting  $\epsilon_\infty = \epsilon$ , the best tolerance we would expect is  $\epsilon$  (tolerance for the simulation)

$\implies n \leq -\frac{\tau}{T} \ln(\epsilon)$ , and using LEMMA 2.1

$$\implies n < \frac{\alpha}{|\alpha|} \left( \frac{R_T}{T} C \ln(\epsilon) \right) \frac{1}{\kappa} : \alpha < 0$$

□

**Remark B.1.** We have two RCR outlet in our simulation model. Defining  $\bar{Q} = \frac{1}{T} \int_0^T Q(t) dt$  as the time-averaged mean flow and splitting the flow along the two outlets according to murray's law as

$$\bar{Q}_1 = \frac{D_1^n \bar{Q}}{D_1^n + D_2^n} \quad \text{and} \quad \bar{Q}_2 = \frac{D_2^n \bar{Q}}{D_1^n + D_2^n} \quad (\text{B7})$$

Within the context of equation (B7),  $D_1$  represents the diameter of Outlet 1, while  $D_2$  signifies the diameter of Outlet 2. For the pulmonary artery, we set the value of  $n$  to 2.3. The subsequent analysis aligns with the previously described methodology, and it is applied to assess the number of simulation cycles needed to attain periodicity.

## Appendix C Comment on Mechanobiological Score (MS)

As indicated in the article, it is noteworthy that MS exhibits a preference for lower values derived from OSI and TAWSS. This valuable insight can be effectively harnessed to elucidate adverse PEEP (Positive End-Expiratory Pressure) settings. **Fig. C1** provides visual evidence of the distribution of MS values for OLA and HI, which closely mirrors the baseline conditions and resembles the OSI patterns. However, a distinct departure is observed in the case of the Collapse condition (**Fig. C1 D**). This deviation can be attributed to the abnormal decrease in TAWSS values, indicating a deficiency in mechanical stimulation experienced by the blood elements. Consequently, this critical information serves as a primary screening tool to exercise caution when considering specific PEEP configurations.

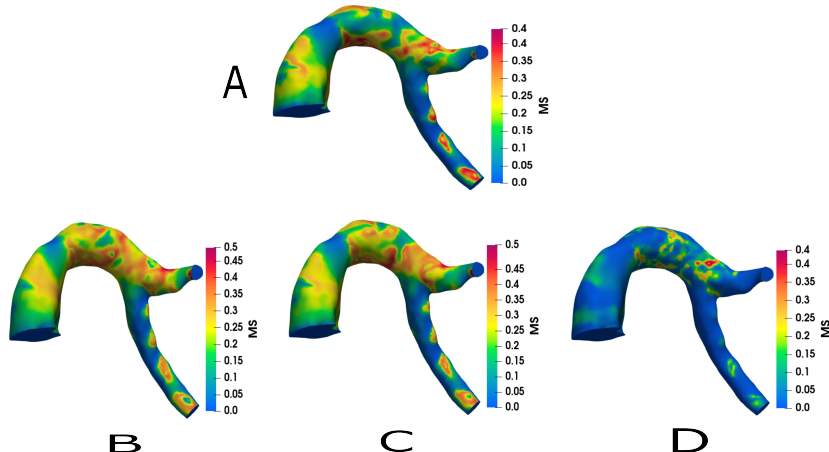


**Fig. C1:** Visualization of the distribution of MS for one subject 2459 A) Baseline condition B) Hyperinflation (HI) C) Open lung approach (OLA) and D) Collapse (COL)

## References

- [1] Ware, L.B., Matthay, M.A.: The acute respiratory distress syndrome **342**(18), 1334–1349 <https://doi.org/10.1056/NEJM200005043421806> . Accessed 2023-03-11
- [2] Sinha, P., Calfee, C.S., Cherian, S., Brealey, D., Cutler, S., King, C., Killick, C., Richards, O., Cheema, Y., Bailey, C., Reddy, K., Delucchi, K.L., Shankar-Hari, M., Gordon, A.C., Shyamsundar, M., O’Kane, C.M., McAuley, D.F., Szakmany, T.: Prevalence of phenotypes of acute respiratory distress syndrome in critically ill patients with COVID-19: a prospective observational study **8**(12), 1209–1218 [https://doi.org/10.1016/S2213-2600\(20\)30366-0](https://doi.org/10.1016/S2213-2600(20)30366-0) . Accessed 2022-12-20
- [3] Ramrez, P., Gordn, M., Martn-Cerezuela, M., Villarreal, E., Sancho, E., Padrs, M., Frasquet, J., Leyva, G., Molina, I., Barrios, M., Gimeno, S., Castellanos, .: Acute respiratory distress syndrome due to COVID-19. clinical and prognostic features from a medical critical care unit in valencia, spain **45**(1), 27–34 <https://doi.org/10.1016/j.medin.2020.06.015> . Accessed 2022-12-20
- [4] Sieren, M.M., Berlin, C., Oechtering, T.H., Hunold, P., Drmann, D., Barkhausen, J., Frydrychowicz, A.: Comparison of 4d flow MRI to 2d flow MRI in the pulmonary arteries in healthy volunteers and patients with pulmonary hypertension **14**(10), 0224121 <https://doi.org/10.1371/journal.pone.0224121> . Accessed 2022-12-20
- [5] Cheng, C.P., Herfkens, R.J., Taylor, C.A., Feinstein, J.A.: Proximal pulmonary

artery blood flow characteristics in healthy subjects measured in an upright posture using MRI: the effects of exercise and age **21**(6), 752–758 <https://doi.org/10.1002/jmri.20333>

- [6] Tang, B.T., Pickard, S.S., Chan, F.P., Tsao, P.S., Taylor, C.A., Feinstein, J.A.: Wall shear stress is decreased in the pulmonary arteries of patients with pulmonary arterial hypertension: An imagebased, computational fluid dynamics study **2**(4), 470–476 <https://doi.org/10.4103/2045-8932.105035> . Accessed 2022-12-20
- [7] Dyverfeldt, P., Bissell, M., Barker, A.J., Bolger, A.F., Carlhll, C.-J., Ebbers, T., Francios, C.J., Frydrychowicz, A., Geiger, J., Giese, D., Hope, M.D., Kilner, P.J., Kozerke, S., Myerson, S., Neubauer, S., Wieben, O., Markl, M.: 4d flow cardiovascular magnetic resonance consensus statement **17**(1), 72 <https://doi.org/10.1186/s12968-015-0174-5> . Accessed 2023-03-27
- [8] Acosta, S., Puelz, C., Rivire, B., Penny, D.J., Brady, K.M., Rusin, C.G.: Cardiovascular mechanics in the early stages of pulmonary hypertension: a computational study **16**(6), 2093–2112 <https://doi.org/10.1007/s10237-017-0940-4> . Accessed 2022-12-20
- [9] Chern, M.-J., Wu, M.-T., Her, S.-W.: Numerical study for blood flow in pulmonary arteries after repair of tetralogy of fallot **2012**, 1–18 <https://doi.org/10.1155/2012/198108> . Accessed 2022-12-20
- [10] Esmaily Moghadam, M., Vignon-Clementel, I.E., Figliola, R., Marsden, A.L.: A modular numerical method for implicit 0d/3d coupling in cardiovascular finite element simulations **244**, 63–79 <https://doi.org/10.1016/j.jcp.2012.07.035> . Accessed 2022-12-20
- [11] Santos, A., Lucchetta, L., Monge-Garcia, M.I., Borges, J.B., Tusman, G., Hedenstierna, G., Larsson, A., Suarez-Sipmann, F.: The open lung approach improves pulmonary vascular mechanics in an experimental model of acute respiratory distress syndrome: **45**(3), 298–305 <https://doi.org/10.1097/CCM.0000000000002082> . Accessed 2022-12-20
- [12] Lpez-Linares Romn, K., La Bruere, I., Onieva, J., Andresen, L., Qvortrup Holsting, J., Rahaghi, F.N., Maca, I., Gonzlez Ballester, M.A., San Jos Estepar, R.: 3d pulmonary artery segmentation from CTA scans using deep learning with realistic data augmentation. In: Stoyanov, D., Taylor, Z., Kainz, B., Maicas, G., Beichel, R.R., Martel, A., Maier-Hein, L., Bhatia, K., Vercauteren, T., Oktay, O., Carneiro, G., Bradley, A.P., Nascimento, J., Min, H., Brown, M.S., Jacobs, C., Lassen-Schmidt, B., Mori, K., Petersen, J., San Jos Estpar, R., Schmidt-Richberg, A., Veiga, C. (eds.) Image Analysis for Moving Organ, Breast, and Thoracic Images vol. 11040, pp. 225–237. Springer. [https://doi.org/10.1007/978-3-030-00946-5\\_23](https://doi.org/10.1007/978-3-030-00946-5_23) . Series Title: Lecture Notes in Computer Science. [http://link.springer.com/10.1007/978-3-030-00946-5\\_23](http://link.springer.com/10.1007/978-3-030-00946-5_23) Accessed 2023-02-03

- [13] FLIPPER. <https://www.graphics.rwth-aachen.de/software/openflipper/>
- [14] TET. Weierstrass Institute
- [15] VMTK
- [16] Updegrove, A., Wilson, N.M., Merkow, J., Lan, H., Marsden, A.L., Shadden, S.C.: SimVascular: An open source pipeline for cardiovascular simulation **45**(3), 525–541 <https://doi.org/10.1007/s10439-016-1762-8> . Accessed 2023-02-07
- [17] Westerhof, N., Bosman, F., De Vries, C.J., Noordergraaf, A.: Analog studies of the human systemic arterial tree **2**(2), 121–143 [https://doi.org/10.1016/0021-9290\(69\)90024-4](https://doi.org/10.1016/0021-9290(69)90024-4) . Accessed 2022-12-20
- [18] Chnafa, C., Brina, O., Pereira, V.M., Steinman, D.A.: Better than nothing: A rational approach for minimizing the impact of outflow strategy on cerebrovascular simulations **39**(2), 337–343 <https://doi.org/10.3174/ajnr.A5484> . Accessed 2022-12-20
- [19] Vignon-Clementel, I.E., Alberto Figueroa, C., Jansen, K.E., Taylor, C.A.: Outflow boundary conditions for three-dimensional finite element modeling of blood flow and pressure in arteries **195**(29), 3776–3796 <https://doi.org/10.1016/j.cma.2005.04.014> . Accessed 2022-12-20
- [20] Schulz-Menger, J., Bluemke, D.A., Bremerich, J., Flamm, S.D., Fogel, M.A., Friedrich, M.G., Kim, R.J., Knobelsdorff-Brenkenhoff, F., Kramer, C.M., Pennell, D.J., Plein, S., Nagel, E.: Standardized image interpretation and post-processing in cardiovascular magnetic resonance - 2020 update: Society for cardiovascular magnetic resonance (SCMR): Board of trustees task force on standardized post-processing **22**(1), 19 <https://doi.org/10.1186/s12968-020-00610-6> . Accessed 2022-12-20
- [21] Di Achille, P., Tellides, G., Figueroa, C.A., Humphrey, J.D.: A haemodynamic predictor of intraluminal thrombus formation in abdominal aortic aneurysms **470**(2172), 20140163 <https://doi.org/10.1098/rspa.2014.0163> . Accessed 2022-12-20
- [22] Ku, D.N., Giddens, D.P., Zarins, C.K., Glagov, S.: Pulsatile flow and atherosclerosis in the human carotid bifurcation. positive correlation between plaque location and low oscillating shear stress. **5**(3), 293–302 <https://doi.org/10.1161/01.ATV.5.3.293> . Accessed 2022-12-20
- [23] Wang, H., Uhlmann, K., Vedula, V., Balzani, D., Varnik, F.: Fluid-structure interaction simulation of tissue degradation and its effects on intra-aneurysm hemodynamics **21**(2), 671–683 <https://doi.org/10.1007/s10237-022-01556-7> . Accessed 2022-12-20

- [24] Bian, C., Xu, G., Wang, J., Ma, J., Xiang, M., Chen, P.: Hypercholesterolaemic serum increases the permeability of endothelial cells through zonula occludens-1 with phosphatidylinositol 3-kinase signaling pathway **2009**, 1–5 <https://doi.org/10.1155/2009/814979> . Accessed 2022-12-20
- [25] Chiu, J.J., Wung, B.S., Shyy, J.Y.J., Hsieh, H.J., Wang, D.L.: Reactive oxygen species are involved in shear stress-induced intercellular adhesion molecule-1 expression in endothelial cells **17**(12), 3570–3577 <https://doi.org/10.1161/01.ATV.17.12.3570> . Accessed 2023-03-11
- [26] Chappell, D.C., Varner, S.E., Nerem, R.M., Medford, R.M., Alexander, R.W.: Oscillatory shear stress stimulates adhesion molecule expression in cultured human endothelium **82**(5), 532–539 <https://doi.org/10.1161/01.RES.82.5.532> . Accessed 2023-03-11
- [27] Meng, H., Tutino, V.M., Xiang, J., Siddiqui, A.: High WSS or low WSS? complex interactions of hemodynamics with intracranial aneurysm initiation, growth, and rupture: Toward a unifying hypothesis **35**(7), 1254–1262 <https://doi.org/10.3174/ajnr.A3558> . Accessed 2023-03-11
- [28] Ventilation with lower tidal volumes as compared with traditional tidal volumes for acute lung injury and the acute respiratory distress syndrome **342**(18), 1301–1308 <https://doi.org/10.1056/NEJM20005043421801> . Accessed 2022-12-20
- [29] Hoffman, J.: Dynamic subgrid modelling for time dependent convection-diffusion-reaction equations with fractal solutions **40**(3), 583–592 <https://doi.org/10.1002/fld.304> . Accessed 2023-02-07
- [30] svSolver
- [31] Marsden, A.L., Esmaily-Moghadam, M.: Multiscale modeling of cardiovascular flows for clinical decision support **67**(3), 030804 <https://doi.org/10.1115/1.4029909> . Accessed 2022-12-20
- [32] Westerhof, N., Elzinga, G., Sipkema, P.: An artificial arterial system for pumping hearts. Journal of Applied Physiology **31**(5), 776–781 (1971) <https://doi.org/10.1152/jappl.1971.31.5.776>
- [33] Stergiopoulos, N., Young, D.F., Rogge, T.R.: Computer simulation of arterial flow with applications to arterial and aortic stenoses. Journal of Biomechanics **25**(12), 1477–1488 (1992) [https://doi.org/10.1016/0021-9290\(92\)90060-e](https://doi.org/10.1016/0021-9290(92)90060-e)
- [34] Womersley, J.R.: Oscillatory Flow in Arteries: the Constrained Elastic Tube as a Model of Arterial Flow and Pulse Transmission. Physics in Medicine and Biology **2**(2), 178–187 (1957) <https://doi.org/10.1088/0031-9155/2/2/305> . Accessed 2023-10-11

- [35] Pfaller, M.R., Pham, J., Wilson, N.M., Parker, D.W., Marsden, A.L.: On the Periodicity of Cardiovascular Fluid Dynamics Simulations. *Annals of Biomedical Engineering* **49**(12), 3574–3592 (2021) <https://doi.org/10.1007/s10439-021-02796-x>